Article

Enhanced Hydrogen Storage Performance of MgH$_2$ by the Catalysis of a Novel Intersected Y$_2$O$_3$/NiO Hybrid

Yushan Liu [1], Shun Wang [1], Zhenglong Li [2,*], Mingxia Gao [1,*], Yongfeng Liu [1], Wenping Sun [1] and Hongge Pan [1]

[1] State Key Laboratory of Silicon Materials and School of Materials Science and Engineering, Zhejiang University, Hangzhou 310027, China; liuys_stu@163.com (Y.L.); 11726036@zju.edu.cn (S.W.); mselyf@zju.edu.cn (Y.L.); wenpingsun@zju.edu.cn (W.S.); honggepan@zju.edu.cn (H.P.)
[2] Institute of Science and Technology for New Energy, Xi'an Technological University, Xi'an 710021, China
* Correspondence: lizhenglong@xatu.edu.cn (Z.L.); gaomx@zju.edu.cn (M.G.)

Abstract: MgH$_2$ is one of the most promising hydrogen storage materials due to its high hydrogen storage capacity and favorable reversibility, but it suffers from stable thermodynamics and poor dynamics. In the present work, an intersected Y$_2$O$_3$/NiO hybrid with spherical hollow structure is synthesized. When introduced to MgH$_2$ via ball-milling, the Y$_2$O$_3$/NiO hollow spheres are crushed into ultrafine particles, which are homogenously dispersed in MgH$_2$, showing a highly effective catalysis. With an optimized addition of 10 wt% of the hybrid, the initial dehydrogenation peak temperature of MgH$_2$ is reduced to 277 °C, lowered by 109 °C compared with that of the bare MgH$_2$, which is further reduced to 261 °C in the second cycle. There is ca. 6.6 wt% H$_2$ released at 275 °C within 60 min. For the fully dehydrogenation product, hydrogenation initiates at almost room temperature, and a hydrogenation capacity of 5.9 wt% is achieved at 150 °C within 150 min. There is still 5.2 wt% H$_2$ desorbed after 50 cycles at a moderate cyclic condition, corresponding to the capacity retention of 79.2%. The crystal structure and morphology of the Y$_2$O$_3$/NiO hybrid is well preserved during cycling, showing long-term catalysis to the hydrogen storage of MgH$_2$. The Y$_2$O$_3$/NiO hybrid also inhibits the agglomeration of MgH$_2$ particles during cycling, favoring the cyclic stability.

Keywords: MgH$_2$; hydrogen storage; Y$_2$O$_3$/NiO hybrid; catalysis; kinetics; cyclic stability

1. Introduction

Hydrogen is considered to be one of the most promising clean energy carriers, while safe, efficient and low-cost storage of hydrogen is the key bottleneck technology for large-scale application of hydrogen energy to date [1–3]. MgH$_2$ has attracted much attention as a hydrogen storage material due to its advantages of good reversibility, high mass hydrogen storage density (7.6 wt%), and low cost [3–6]. MgH$_2$ prepared from waste Mg-alloys also show favorable possibility for hydrogen storage [5,6], offering more opportunities to lower the cost. However, the high thermal stability of MgH$_2$ (ΔH = 75 kJ·mol^{-1} H$_2$) and the reaction barrier (ΔE = 161 kJ·mol^{-1}) [7] lead to high dehydrogenation temperature, where the peak dehydrogenation temperature is commonly over 360 °C [8], which limit its practical application for hydrogen storage.

Common methods to improve the hydrogen storage performance of MgH$_2$ include alloying [9–18], nanoconfinement [19,20], nano-crystallization [21–26], and catalyst doping [27–35]. Alloying of Mg by combining with other metal elements, such as Al, Ni, and Ge, can produce less stable Mg-based hydrides. However, the introduction of the second metal element commonly leads to large capacity decrease of Mg-based hydrides. One typical example is Mg$_2$NiH$_4$, which has a low theoretical capacity of only 3.6 wt%, though its dehydrogenation temperature is decreased to 255 °C at 1 bar equilibrium H$_2$ pressure [34]. Nano-crystallization is effective in modifying the thermodynamics and kinetics of MgH$_2$, especially the latter [19–26]. For thermodynamic modification, theoretical calculations

suggest that when the grain size of MgH_2 is reduced to 0.9 nm, the decomposition enthalpy is only 63 kJ mol^{-1} H$_2$, corresponding to a theoretical desorption temperature of only 200 °C [36]. The reduced particle size results in a shortened diffusion distance, hence improving the hydrogen de-/absorption kinetics of MgH_2 leading to a 50% decrease in activation energy [21]. However, direct synthesis of MgH_2 nanoparticles smaller than 20 nm is so far difficult to achieve due to its high reactivity in nanoscale. In this case, thermodynamic modification by reducing particle size is practically difficult. Nevertheless, MgH_2 nanoparticles tend to grow and agglomerate along with cycles, which leads to severe performance deterioration. The size stability of MgH_2 can be enhanced by confining MgH_2 in porous scaffolds, but the scaffold materials commonly take up considerable amount in the confined systems, i.e., occupy a considerable volume of the system, causing significant capacity loss. For instance, by confining Mg particles in polymethyl methacrylate, a hydrogen absorption capacity of only 4.8 wt% H$_2$ is obtained at 200 °C and 3 MPa H$_2$ [20].

In contrast, catalytic modification of highly active catalysts can improve the kinetic performance of MgH_2 effectively with less capacity loss. For example, the addition of a carbon film coated dual transition metal alloy, $Fe_{0.64}Ni_{0.36}$@C with a core-shell structure, can make Mg absorb hydrogen rapidly within 20 min at 150 °C and 3 MPa H$_2$, with a capacity of 5.8 wt% [27]. A K_2SiF_6 introduced MgH_2 system shows a dehydrogenation capacity of 5.1 wt% in 30 min at 320 °C [32]. Previous studies also show that transition metals [37,38] and metal compounds [39,40] exhibit effective catalysis to MgH_2. Among them, Ni-based catalysts are of particular interest owing to their effective role in promoting the dissociation and combination of hydrogen [41]. For example, the introduction of a type of porous nickel nanowires to MgH_2 results in a decrease of the peak dehydrogenation temperature from 385 to 278 °C [42]. Furthermore, the combination of Ni catalysts with other species is a useful approach in obtaining effective catalysis. It is reported that a self-assembled two-dimensional MXene-Ti_3C_2 loaded with ultra-dispersed Ni nanoparticles (Ni@Ti_3C_2) shows favorable catalysis to MgH_2 on hydrogen storage, which shows superior catalysis to either bare Ni nanoparticles or MXene-Ti_3C_2 [28]. The MgH_2 system added with this Ni@Ti_3C_2 composite can release 5.2 wt% H$_2$ within 15 min at 250 °C and absorb 5.4 wt% H$_2$ within 25 s at 125 °C. In addition to transition metals-based catalysts, rare earth metals and their oxides also show effective catalysis to MgH_2. For instance, Y_2O_3 and Y are also found to play catalytic roles in the hydrogen de/absorption of Mg, and Y_2O_3 shows a more effective catalysis than Y [43]. It is also reported in many studies, many metal oxides have favorable catalytic effects [44–46].

Progress has been obtained on the improvement of the hydrogen storage performance of MgH_2; however, the synthesis of the highly active catalysts seems complicated, such as with the $Fe_{0.64}Ni_{0.36}$@C catalyst, where several synthesis steps and almost 3 days are needed for one period [27], and the catalyst of MXene-Ti_3C_2 needs almost one week for one synthesis period [28]. Some of the other catalysts shows moderate effects on the improvement of MgH_2 [14,19,32], though they can improve the hydrogen storage properties of MgH_2 to some extent. Therefore, developing highly effective catalysts with facile synthesis methods is still highly desired. Y_2O_3 [43] and NiO [44] show catalytic effects on MgH_2, but the effects are moderate. Additionally, incorporation of some different catalysts shows synergistic catalytic effects on Mg-based hydrogen storage materials, such as the incorporation of Y_2O_3 and YH_2 for the $Mg_{0.97}Zn_{0.03}$ solid solution alloy [47], and the incorporation of NiO and Ni for the Mg system [44]. In the present work, we design and synthesize a novel structural intersected Y_2O_3/NiO hybrid by a facile spray sintering method, which shows highly effective catalysis on MgH_2. Compared with some chemical synthesis methods, such as the hydrothermal method [19], which generally has low productivity, the present synthesis method has high productivity, which has the potential for large-scale production. The hybrid shows a spherical hollow structure. By introducing to MgH_2 via ball-milling, the hollow Y_2O_3/NiO spheres are crushed into ultrafine pieces in nanometers, which are homogenously dispersed in MgH_2. With an optimization of the addition of 10 wt% of the intersected hybrid, the MgH_2 system shows

significantly improved hydrogen storage properties. The mechanism of the improved hydrogen storage properties is proposed. The work is hopefully helpful in the composition and structural design of novel catalysts to MgH_2 and other high-performance hydrogen storage materials and for developing synthesis methods of large-scale production.

2. Materials and Methods

2.1. Synthesis of the Intersected Y_2O_3/NiO Hybrid

The synthesis process of the intersected Y_2O_3/NiO hybrid is schematically illustrated in Figure 1, where $Y(C_2H_3O_2)_3\cdot4H_2O$ (Sinopharm, analytical reagent, Beijing, China) and $Ni(C_2H_3O_2)_2\cdot4H_2O$ (Sinopharm, analytical reagent, Beijing, China) are used as the sources of Y_2O_3 and NiO, respectively. A designed molar ratio of 1:1 was used for Y_2O_3 and NiO. Typically, 50.7 g of $Y(C_2H_3O_2)_3\cdot4H_2O$ and 37.4 g of $Ni(C_2H_3O_2)_2\cdot4H_2O$ were added into 1 L of deionized water and mechanically stirred, and then 63 g of citric acid $(HOC(COOH)(CH_2COOH)_2\cdot H_2O$, Sinopharm, analytical reagent, Beijing, China) was added as a complexing agent to prevent metal salt hydrolysis and hydroxide precipitation. The obtained mixture is further mechanically stirred to form a solution. Thereafter, the solution was spray dried with inlet and outlet temperatures of 230 and 100 °C, respectively, and a feeding speed of 1 L/h was used. Subsequently, the spray dried precursor was heated to 900 °C at a heating rate of 3 °C/min in an air atmosphere and dwelled for 10 h. After cooling to room temperature, the intersected Y_2O_3/NiO hybrid with a hollow spherical structure was obtained.

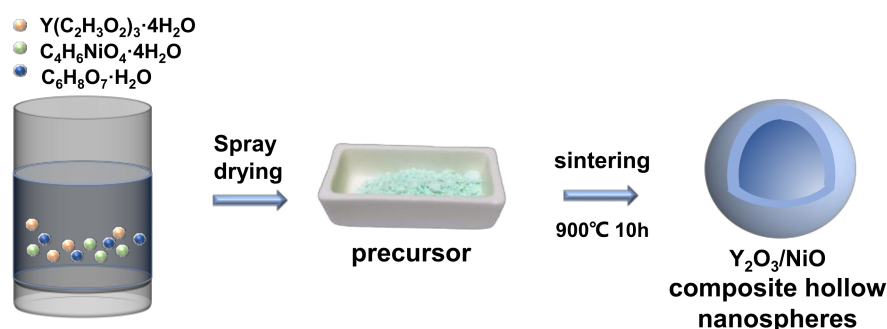**Figure 1.** Schematic illustration of the preparation process of the intersected Y_2O_3/NiO hybrid with spherical hollow structure.

2.2. Preparation of the Y_2O_3/NiO Introduced MgH_2 Systems

MgH_2 used in the present study was synthesized from commercially purchased Mg powder (Macklin, 99.8%, 20~100 mesh, Shanghai, China) by hydrogenating at 340 °C under 50 bar of hydrogen pressure (Jingong Gases, 99.999%, Hangzhou, China,) for 12 h. Thereafter, the as-prepared Y_2O_3/NiO hybrid was introduced into MgH_2 with different amounts by ball milling under 50 bar of hydrogen at 500 rpm for 5 h, where tungsten carbide balls and a ball-to-power ratio of 180:1, which was a conventional and optimized parameter obtained in our group, were used. The obtained systems are denoted as MgH_2-x wt% Y_2O_3/NiO systems (x = 2, 5, 7, 10, 12). For comparison, the commercial Y_2O_3 (Rhawn, 99.99%, 0.5 μm, Shanghai, China) and NiO (Rhawn, 99.5%, 30 nm, Shanghai, China) was also introduced into MgH_2 using the same ball-milling parameters. All MgH_2-related operations were performed in a glove box (Etelux, Lab 2000, Beijing, China) filled with argon (Jingong Gases, 99.999%, Hangzhou, China), with the concentrations of water and oxygen both below 1 PPM.

2.3. Structure and Morphology Characterizations

The phase structures of samples were identified by X-ray diffraction (XRD, Miniflex600, Tokyo, Japan) with the radiation source of Cu Kα (40 kV, 15 mA), where the samples were sealed in a custom-designed container covered with a Scotch tape to prevent air and

moisture contamination during operation. Scanning electron microscope (SEM, Hitachi-4800, Tokyo, Japan) attached with energy dispersive X-ray spectroscopy (EDS) was used to observe the surface morphologies and element distributions of the samples. Morphologies were also analyzed by transmission electron microscope (TEM, Tecnai G2 F20 S-Twin, Hillsboro, OR, USA). The surface compositions of the samples and the chemical states of the corresponding elements were analyzed by X-ray photoelectron spectroscopy (XPS, Escalab 250 Xi, Waltham, MA, USA) with a monochromatic Al Kα X-ray source under a base pressure of 3.7×10^{-10} Torr. The XPS data were calibrated using the adventitious C 1s signal at 284.8 eV as the reference, and binding energy spectra were fitted using XPSPEAK41 software.

2.4. Hydrogen Storage Property Measurements

The hydrogen storage property measurements of the systems were carried out on a home-made Sieverts type apparatus. For non-isothermal dehydrogenation and hydrogenation tests, samples were heated to designed temperatures with a heating rate of 2 °C/min under a primary vacuum and 5 MPa H$_2$ pressure, respectively. For isothermal tests, samples are heated to preset temperatures with a heating rate of 10 °C/min. Isothermal dehydrogenation was also conducted under a primary vacuum. For isothermal hydrogenation, a primary vacuum was used until the preset temperatures were reached, and then 5 MPa of H$_2$ was loaded instead of the vacuum. The cyclic stability was measured with an isothermal regime of dehydrogenation at 300 °C for 40 min in an initial vacuum and hydrogenation at 300 °C for 20 min in 5 MPa H$_2$, where the periods only denote the isothermal ones. The thermodynamic properties of the systems were studied by differential scanning calorimetry (DSC, Netzsch, Selb, Germany). Thermodynamic enthalpies of the systems were calculated by integrating the peak areas of DSC curves through Proteus Analysis Software provided by Netzsch. The kinetic performance was evaluated based on the dehydrogenation apparent activation energy (E_a), which was obtained according to the Kissinger method [48], as shown in Equation (1).

$$\ln\left(\frac{\beta}{T_m^2}\right) = -\frac{E_a}{RT_m} + C \tag{1}$$

where β is the heating rate, T_m is the dehydrogenation peak temperature at corresponding heating rate, R is the gas constant, and C is a constant which shows no specific meaning in the calculation of apparent activation energy. In this work, a home-made temperature programmed desorption (TPD) apparatus was used, which can intuitively obtain the onset, peak, and ending dehydrogenation temperatures at different heating rates.

3. Results

3.1. Structures and Morphologies of the Y$_2$O$_3$/NiO Hybrid and the MgH$_2$-xwt%Y$_2$O$_3$/NiO Systems

Figure 2 shows the XRD patterns of the as-prepared Y$_2$O$_3$/NiO hybrid, the raw MgH$_2$, and a representative MgH$_2$-x wt% Y$_2$O$_3$/NiO system with x of 10. It seems that, for the as-prepared Y$_2$O$_3$/NiO hybrid, only sharp peaks from Y$_2$O$_3$ (PDF-# 43-0661) and NiO (PDF-# 44-1159) are detected, indicating that the synthesized product is composed of Y$_2$O$_3$ and NiO with high crystallinity. For the as-milled MgH$_2$-10 wt% Y$_2$O$_3$/NiO system, there are still Y$_2$O$_3$ and NiO detected, besides the phase of MgH$_2$. The result suggests that there is no chemical reaction occurring during ball-milling process. However, the diffraction peak intensities of MgH$_2$, Y$_2$O$_3$, and NiO are all obviously weakened after ball milling compared with those of their as-prepared states, indicating reduced particle size and/or lowered crystallinity.
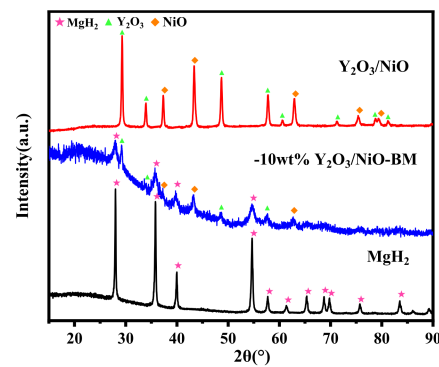
Figure 2. XRD patterns of the as-prepared Y_2O_3/NiO hybrid, the MgH_2-10wt% Y_2O_3/NiO system and the pristine MgH_2.

Figure 3a shows the SEM image of the Y_2O_3/NiO hybrid. It is seen that the hybrid has a spherical structure with coarse surface in size of micron and sub-micron level. A hollow structure can be observed from the crushed particle. EDS element mapping results of one selected nanosphere, as presented in Figure 3b–e, show that Y, Ni, and O elements are uniformly distributed in the whole nanosphere. TEM observation (Figure 3f) confirms that the hybrid spheres have internal hollows. Moreover, the high-resolution TEM (HRTEM) analysis (Figure 3g) clearly shows that there are crystal grains with interplanar spacing of 0.306 nm, corresponding to lattice fringes of the (222) plane for Y_2O_3, and interplanar spacing of 0.208 nm, corresponding to the lattice fringes of the (012) plane of NiO, which are interactively grown, forming an intersected structure. Combining the EDS and HRTEM analyses, it is thus obtained that the prepared Y_2O_3/NiO hybrid is composed of interactively grown Y_2O_3 and NiO crystal grains.
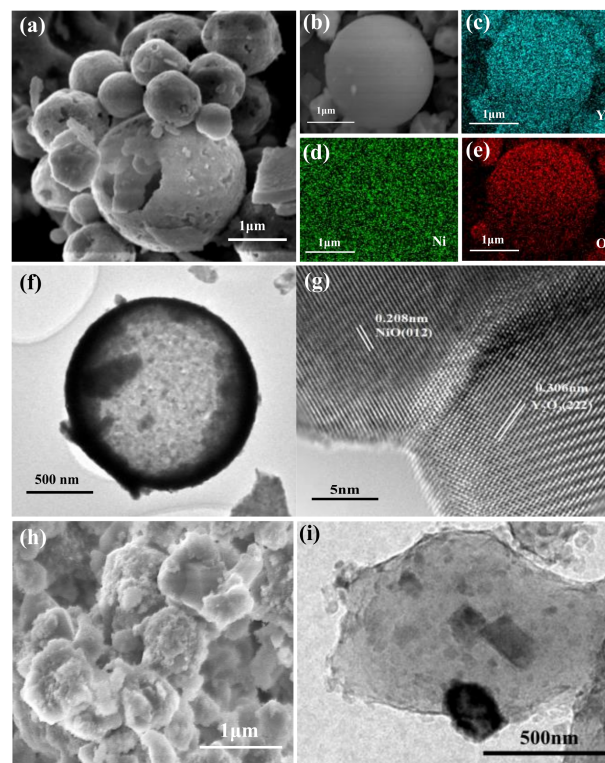

Figure 3. (**a**) SEM image; (**b**–**e**) EDS mappings of Y, Ni, and O elements; (**f**) TEM image; and (**g**) HRTEM image of the as-prepared Y_2O_3/NiO hybrid. (**h**) SEM and (**i**) TEM images of the MgH_2-10 wt% Y_2O_3/NiO system.

SEM observation of the MgH_2-10 wt% Y_2O_3/NiO system as a representative is also conducted, as shown in Figure 3h. It is seen that the particle size of the system is not evidently different from that of the bare MgH_2, which is performed for a same ball-milling regime (Figure S1). The MgH_2-10 wt% Y_2O_3/NiO system has a size range of 300–900 nm with most particles distributing between 500–700 nm. The spherical structure of the as-synthesized Y_2O_3/NiO hybrid is not observed after the ball milling. Further TEM analysis, as presented in Figure 3i, shows image of dark-gray fragments in size of nanometers dispersing in light-gray matrix, which indicates that the fine dark-gray fragments in size around 100–200 nm are the Y_2O_3/NiO hybrid, and the matrix is MgH_2. It is obtained that the hollow nanospheres of Y_2O_3/NiO are crushed into fine fragments and are well dispersed in the MgH_2 matrix.

3.2. Hydrogen Storage Performance of the MgH_2-xwt%Y_2O_3/NiO Systems

Figure 4a shows the TPD curves of the MgH_2-x wt% Y_2O_3/NiO systems with that of the pristine MgH_2 for comparison. It is seen that a small amount addition of the Y_2O_3/NiO hybrid can significantly reduce the onset and the main dehydrogenation temperatures of MgH_2. All the composite systems show a two-step dehydrogenation process, where the first step in the relatively low temperature range is the major one, which shows sharp peaks, and the subsequent step in the comparatively high temperature range is a minor one, which is partially overlapped with the major one, occurring as a shoulder peak. The onset peak dehydrogenation temperatures of the composite systems are around 220 °C, and the peak temperatures of the first step are in the range of 280–310 °C, where a higher addition of the hybrid of Y_2O_3/NiO in the range of 2–10 wt% corresponds to a lower peak temperature. Further increasing the addition of Y_2O_3/NiO to 12 wt% only results in a little reduction in the peak temperature. The second-step dehydrogenation occurs in the temperature range of 320–350 °C. In contrast, the bare MgH_2 releases H_2 with onset and peak dehydrogenation temperatures as high as 350 and 386 °C, respectively. As a representative, the MgH_2-10 wt% Y_2O_3/NiO system shows low onset and peak dehydrogenation temperatures of ca. 220 and 279 °C, respectively, which are lowered by 130 and 107 °C, compared with those of the pristine MgH_2 (350 and 386 °C, respectively). The dehydrogenation peak temperature of the MgH_2-10 wt% Y_2O_3/NiO system is ca. 144 °C and 156 °C lower than that of Y_2O_3 and Y-doped MgH_2 systems [43], and the dehydrogenation kinetics is better than that of the Pt-doped MgH_2 system which releases less than 2 wt% of hydrogen at 275 °C for 200 min, while the amount of hydrogen released of the present system reaches 6.2 wt% under the same condition [49].

Figure 4b shows the non-isothermal dehydrogenation curves of the MgH_2-x wt% Y_2O_3/NiO systems. A two-step dehydrogenation process is also shown, which is consistent with the result from the TPD result, where the first step is the main one and the second one is the minor one. The occurrence of the second step is supposed due to the less efficient catalytic effect on the Y_2O_3/NiO hybrid to MgH_2, which may be due to the existence of large Y_2O_3/NiO particles that are heterogeneously mixed with MgH_2. The main dehydrogenation process is completed at a close temperature range of ca. 260–300 °C for the systems with the addition of Y_2O_3/NiO. In addition, with the increasing amount of the Y_2O_3/NiO hybrid introduced, the system shows lower main ending dehydrogenation temperatures. As an overall, dehydrogenation is mostly completed upon heating to 350 °C for all the composite systems. In comparison, completing the dehydrogenation needs a high temperature over 400 °C for bare MgH_2. Moreover, the main dehydrogenation curves move to lower temperature ranges as overall with the increasing amounts of the Y_2O_3/NiO hybrid introduced, except that the two of the systems with 10 and 12 wt% Y_2O_3/NiO additions are almost overlapped. Nevertheless, the former shows a slightly higher dehydrogenation capacity in the followed second step.
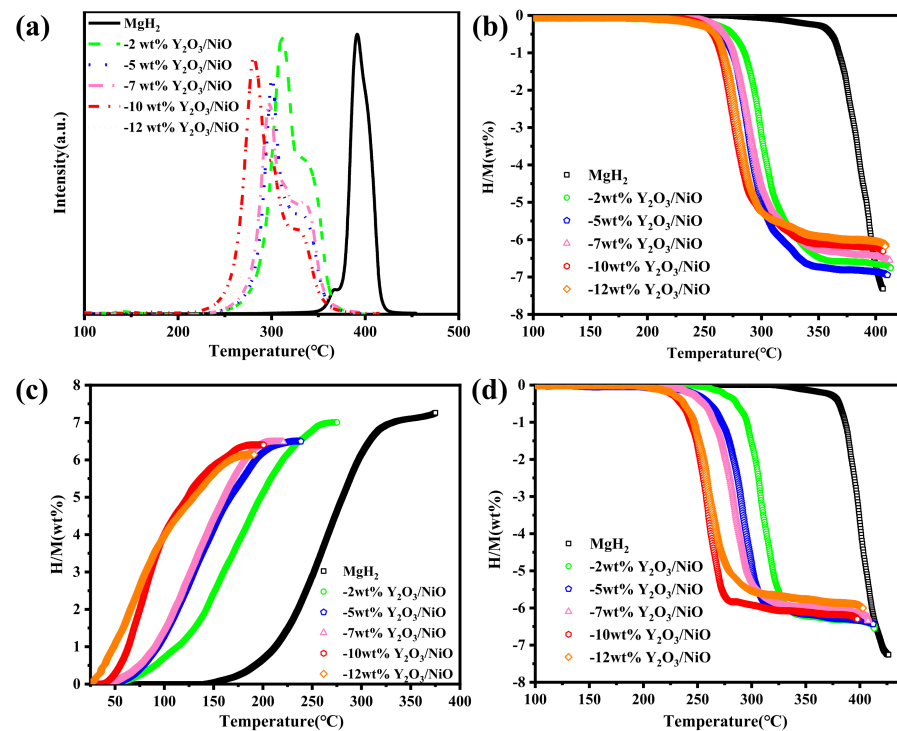
Figure 4. (**a**) TPD, (**b**) the first dehydrogenation, (**c**) the hydrogenation of the dehydrogenation products of (**b**), and (**d**) the second dehydrogenation curves of the MgH_2-*x*wt% Y_2O_3/NiO systems.

Among the composite systems, the MgH_2-10 wt% Y_2O_3/NiO one shows the highest hydrogen capacity of 5.2 wt% upon heating to 300 °C. Further increasing the dehydrogenation temperature results in more hydrogen release for the systems with less amounts of Y_2O_3/NiO addition as their higher theoretical hydrogen storge capacity. The system with 5 wt% Y_2O_3/NiO addition can release more amount of hydrogen compared with the others when the dehydrogenation temperature is over 320 °C, and a capacity of 6.8 wt% H_2 is achieved upon heating to 350 °C. The peak dehydrogenation temperatures of the systems obtained by making the differentiation of the dehydrogenation curves is highly consistent with the TPD results as shown in Figure S2a. The onset dehydrogenation temperature of the present MgH_2 doped with 10 wt% Y_2O_3/NiO is comparable with that of a Mn-doped MgH_2 system [50] and is 35 and 50 °C lower than those of the FeCoNi@GS doped [51] and $HfCl_4$ doped [52] MgH_2 systems, respectively. Moreover, the amount of hydrogen released upon heating to 300 °C of the present work (5.2 wt% H_2) is also much higher than that of the two works, where the FeCoNi@GS doped MgH_2 system only shows a dehydrogenation capacity less than 3 wt% at the same temperature.

Figure 4c shows the hydrogenation curves of the systems which are pre-dehydrogenated to 410 °C, as noted in Figure 4b. It is seen that the hydrogenation temperatures of the composite systems are significantly lowered by the introduction of the Y_2O_3/NiO hybrid. For the composite systems, the hydrogen absorption takes place at temperatures lower than 50 °C. Especially for the systems with 10 and 12 wt% Y_2O_3/NiO additions, the hydrogen absorption takes place at room temperature, whereas for the bare MgH_2, hydrogen absorption takes place at ca. 150 °C. The systems added with 5–10 wt% Y_2O_3/NiO can absorb almost the same amount of H_2, 6.3–6.5 wt%, in the hydrogenation temperature range of 25–235 °C. The system with 2 wt% Y_2O_3/NiO shows somewhat higher capacity but, accordingly, a higher hydrogenation temperature. In addition, the system with 12 wt% Y_2O_3/NiO addition turns out to have a slightly lower hydrogenation temperature compared with the one with 10 wt% Y_2O_3/NiO, but the hydrogen absorption capacity of the former is lower than that of the latter. As a representative, a saturated value of 6.3 wt% H_2 can be absorbed for the MgH_2-10 wt% Y_2O_3/NiO system when the temperature reaches 180 °C.

Figure 4d shows the dehydrogenation curves of the hydrogenated systems as noted in Figure 4c. It is found that, overall, a higher amount of Y_2O_3/NiO introduced results in a lower dehydrogenation temperature for the system, which shows similar regulation as the initial dehydrogenation process. Moreover, the main dehydrogenation for the systems with different additions of Y_2O_3/NiO is in a larger temperature range compared with that of the initial one. The dehydrogenation curves of the systems with 10 and 12 wt% Y_2O_3/NiO almost overlap in the main dehydrogenation process. However, less amount of H_2 can be released in the following high temperature range for the latter. For the MgH_2-10 wt% Y_2O_3/NiO system, a capacity of 5.0 wt% is obtained upon heating to 280 °C, where the main dehydrogenation is almost complete. The capacity is significantly higher than that of the first around dehydrogenation at 280 °C, where a capacity of only 3.1 wt% is obtained (Figure 4b). There is evident decrease in the onset, main, and ending dehydrogenation temperatures for the system with 10 wt% Y_2O_3/NiO for the second dehydrogenation compared with the data in the initial one, with onset, peak, and ending temperatures of ca. 215, 261, and 327 °C, respectively, as obtained from the differentiation of the second cycle dehydrogenation curve (Figure S2b), lowered by 5, 16, and 19 °C compared with those of the initial dehydrogenation. Differences in the dehydrogenation temperature between the second and initial dehydrogenation are also observed for the other systems. The dehydrogenation temperature of the system with 5 wt% Y_2O_3/NiO addition for the second cycle is a little lower than that of the first cycle, while the capacity is much lower than that of the initial cycle. In addition, the second dehydrogenation temperature of the system with 2 wt% Y_2O_3/NiO is even a little higher than that of the first cycle. The reason for these differences on the dehydrogenation temperatures of the first and second cycles will be discussed in the following section.

Considering that the MgH_2-10 wt% Y_2O_3/NiO system shows an overall favorable performance of low dehydrogenation and hydrogenation temperatures, less capacity loss and high reversibility, further kinetics and cyclic studies are performed on this system. For comparison, parallel tests are also performed for the bare MgH_2, the results of which are also shown. Figure 5a shows the isothermal dehydrogenation curves of the MgH_2-10 wt% Y_2O_3/NiO system as well as the bare MgH_2 at different temperatures. The record of the amount of H_2 released starts when the temperature reaches the designed one. It is seen that the hydrogen desorption rate of MgH_2 is greatly enhanced by the introduction of the Y_2O_3/NiO hybrid. When the temperature reaches 275 °C, 3.7 wt% H_2 is already released, and following a 15-min dwelling, a capacity of 6.0 wt% is reached. This isothermal property is comparable to that of Mn-doped MgH_2 system [50]. In addition, a total amount of 6.6 wt% H_2 is released when the isothermal period is further extended to 60 min. In contrast, there is almost no H_2 released for the bare MgH_2 upon heating to 275 °C, and there is only 1.2 wt% hydrogen released even after the isothermal period is extended to 160 min.
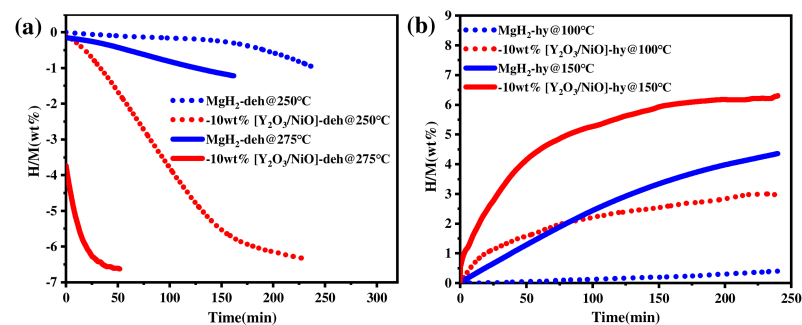

Figure 5. (**a**) Isothermal dehydrogenation and (**b**) hydrogenation curves at different temperatures of the MgH_2-10wt% Y_2O_3/NiO system as well as the bare MgH_2. For hydrogenation testing, the samples are pre-dehydrogenated upon heating to 410 °C and H_2 of 5 MPa is loaded when the temperature reaches the designed one.

At a lower isothermal temperature of 250 °C, a dehydrogenation capacity of 6.3 wt% H_2 is obtained for an isothermal period of 225 min for the MgH_2-10 wt% Y_2O_3/NiO system, whereas there is less than 1 wt% H_2 released for the bare MgH_2 in the same isothermal period. Since much lower isothermal dehydrogenation temperatures are used for the present system than those used in the FeCoNi@GS doped [51] and $HfCl_4$ doped [52] systems, the reaction kinetics cannot be quantitatively compared, but the dehydrogenation kinetics of the present work is superior to that of the MgH_2 system catalyzed with Pt [49] and is also superior to that of the system catalyzed by TiC_x@C [53] in terms of the same test temperatures of 275 and 250 °C, respectively.

Isothermal hydrogenation tests at different temperatures with a H_2 pressure of 5 MPa are also performed for the MgH_2-10 wt% Y_2O_3/NiO system as well as the bare MgH_2, which are pre-dehydrogenated upon heating to 410 °C as noted in Figure 4b. H_2 is loaded when the temperature reaches the designed one. The results are shown in Figure 5b. It is seen that the hydrogen absorption kinetics of MgH_2 is also significantly improved by the introduction of the Y_2O_3/NiO hybrid. At an isothermal temperature of 150 °C, a hydrogen absorption capacity of 4.2 wt% is achieved within 50 min for the MgH_2-10 wt% Y_2O_3/NiO system, and a capacity of 5.9 wt% is achieved when further extending the isothermal period to 150 min. In addition, further extending the isothermal period to 200 min, there will be a slightly higher amount of H_2 absorbed, whereas over 200 min is needed for the bare MgH_2 to achieve a hydrogenation capacity of 4.4 wt%. Moreover, even at a low temperature of 100 °C, a hydrogen absorption capacity of 3.0 wt% can be reached for the MgH_2-10 wt% Y_2O_3/NiO system within 240 min, whereas no obvious hydrogen uptake is observed for the bare MgH_2. It is obtained that the intersected Y_2O_3/NiO hybrid exhibits highly effective bidirectional catalysis on both dehydrogenation and hydrogenation kinetics of MgH_2.

Figure 6 shows the cyclic dehydrogenation and hydrogenation capacities of the MgH_2-10 wt% Y_2O_3/NiO system for 50 cycles. The initial dehydrogenation capacity is 6.5 wt%. A dehydrogenation capacity of 5.2 wt% is maintained for the MgH_2-10 wt% Y_2O_3/NiO system after 50 cycles, corresponding to capacity retention of 79.2%. Close values for hydrogenation capacity are obtained for the same cycle, indicating high reversibility. The average dehydrogenation capacity decay for each cycle in the 50 cycles is only 0.026 wt%. The result demonstrates that the introduction of Y_2O_3/NiO also significantly improves the cyclic stability of MgH_2, of which the hydrogen desorption capacity retention after 50 cycles was only 10.9% as shown in Figure S7.
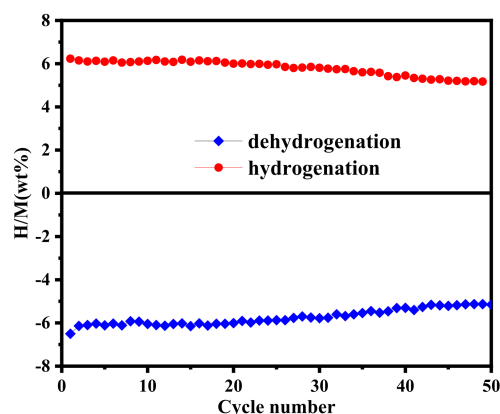

Figure 6. Cyclic dehydrogenation and hydrogenation capacities of the MgH_2-10wt% Y_2O_3/NiO system with a cyclic regime of dehydrogenation at 300 °C for 40 min and hydrogenation at 300 °C and 5 MPa H_2 for 20 min.

As different cyclic regimes are used in different research groups, the cyclic properties from different groups cannot be quantitatively compared. It is still necessary to present some data, such as the Mn-doped MgH_2 system shows the capacity retention of 89% after 20 cycles, maintaining a capacity of 5.72 wt% [49] at a cyclic regime of isothermal

dehydrogenation and hydrogenation (3 MPa) at 275 °C. A capacity of 6.02 wt% remained after 20 cycles for the FeB/CNTs-doped MgH$_2$ system [54], corresponding to the capacity retention of 93% with a cyclic regime of isothermal dehydrogenation at 300 °C (vacuum) and isothermal hydrogenation at 150 °C (5 MPa of H$_2$).

4. Discussion

To investigate the mechanism of the improved hydrogen storage performance of MgH$_2$ by the introduction of the intersected Y$_2$O$_3$/NiO hybrid, the dehydrogenation apparent activation energy (E_a) and the dehydrogenation reaction enthalpy (ΔH_{des}) of the MgH$_2$-10 wt% Y$_2$O$_3$/NiO system are evaluated based on the Kissinger's method and DSC measurement, respectively. Figure 7a shows the Kissinger's plot obtained by fitting the TPD-MS curves of different heating rates, where the E_a value of the MgH$_2$-10 wt% Y$_2$O$_3$/NiO system is calculated to be 86 ± 5 kJ·mol^{-1}, which is 46% lower than 160 ± 10 kJ·mol^{-1} for the bare MgH$_2$. The decreased E_a value indicates a lowered dehydrogenation energy barrier of MgH$_2$ by the introduction of the Y$_2$O$_3$/NiO hybrid, contributing to the improvement of dehydrogenation kinetics. Figure 7b shows the Kissinger's fitting plot of the MgH$_2$-10 wt% Y$_2$O$_3$/NiO system after 50 cycles. It is seen that the E_a value of the composite system only shows a slight increase of 3 kJ·mol^{-1} after cycling, which is extremely small and smaller than 6 kJ·mol^{-1} for the bare MgH$_2$. The result indicates a sustainable catalysis of the Y$_2$O$_3$/NiO hybrid on the kinetics of MgH$_2$.
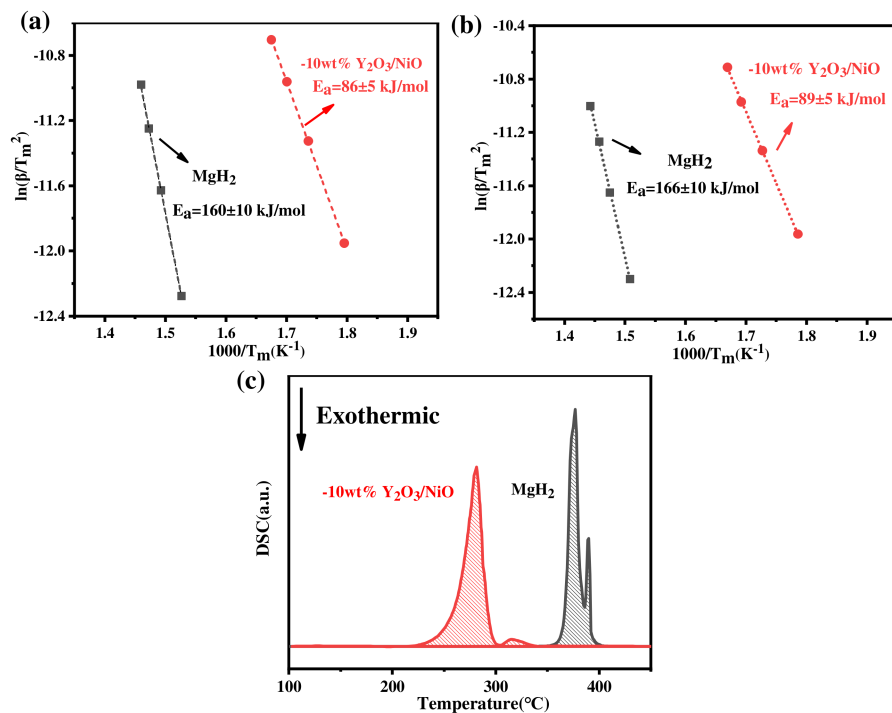

Figure 7. (**a**) Kissinger's fitting plots of the MgH$_2$-10wt% Y$_2$O$_3$/NiO system as well as the bare MgH$_2$ and (**b**) their hydrogenation products after 50 cycles; (**c**) DSC curves of the MgH$_2$-10wt% Y$_2$O$_3$/NiO system as well as the bare MgH$_2$.

Figure 7c shows the DSC curve of the MgH$_2$-10 wt% Y$_2$O$_3$/NiO system. There is a strong endothermic peak observed at 278 °C, ascribed to the dehydrogenation of MgH$_2$. By integrating the peak area, the corresponding ΔH_{des} value is calculated to be 71.9 kJ·mol^{-1} H$_2$, which is close to 73.2 kJ·mol^{-1} H$_2$ of the bare MgH$_2$. This indicates that the introduction of the Y$_2$O$_3$/NiO hybrid almost does not change the thermodynamic behavior of MgH$_2$. It is concluded that the improvement of the hydrogen storage performance of the catalytic system is mainly attributed to kinetic factor.

The XRD patterns of the MgH_2-10 wt% Y_2O_3/NiO system at different dehydrogenation and hydrogenation stages are shown in Figure 8. It is found that MgH_2 and Mg phases interconvert accompanying with the hydrogenation and dehydrogenation processes, while the phases of Y_2O_3 and NiO are always detected in the products either after the first dehydrogenation or after 50th dehydrogenation with no other new phase detected. The result indicates that Y_2O_3 and NiO almost maintain stable in crystal structure during cycling instead of being reduced, which is consistent with the results presented of previous reports [47,55]. Moreover, chemical state analyses of the elements of Y and Ni in the dehydrogenation and hydrogenation stages of the system identified by XPS (Figure S3) show that the chemical states of Y and Ni also remain as Y_2O_3 and NiO, respectively, for their as-milled sates and the dehydrogenation/hydrogenation states of the first and second cycles. Further HRTEM analysis of the dehydrogenation product of the system performed by the regime as noted in Figure 4b shows that there are lattice planes of (200) plane of Y_2O_3 and (101) plane of NiO vaguely observed, which still shows the intersected structure (Figure S4). Although the image is not in a high resolution, as the Y_2O_3/NiO hybrid is high-energy ball-milled and tightly connected with the dehydrogenation product of MgH_2 (Mg), it still can be obtained that the intersected structure is well inherited to the dehydrogenation product. Combining with the results of the aforementioned XRD analysis, it is obtained that the intersected Y_2O_3/NiO hybrid does not participate in the dehydrogenation and hydrogenation reactions of MgH_2, maintaining the states of Y_2O_3 and NiO.

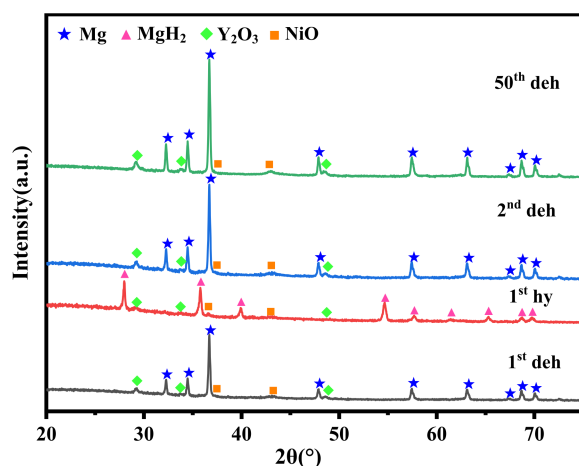**Figure 8.** XRD patterns of the MgH_2-10wt%Y_2O_3/NiO system at different dehydrogenation(deh) and hydrogenation(hy) stages. The first and second cycle dehydrogenation/hydrogenation products are by the regime as noted for Figure 4. The 50th dehydrogenation product is by the regime as noted for Figure 6.

Comparison of the particles size of the systems with low (2 wt%) and high (12 wt%) amount of Y_2O_3/NiO additions as well as the bare MgH_2 at as-milled and initial hydrogenation sates by SEM observation (Figure S5) demonstrates that there is severe particle growth and agglomeration for the bare MgH_2 and for the composite system with low amount (2 wt%) Y_2O_3/NiO addition, whereas there is almost no particle growth for the system introduced with a high (12 wt%) amount of Y_2O_3/NiO, and it seems that there is even a slight particle size decrease. It is reported that cracks are generated in the oxide of MgO during annealing and hydrogenation processes, providing more surface area and active sites and resulting in more pathways for hydrogen diffusion. As a result, the second dehydrogenation temperature is reduced compared with the initial one [56]. In the present work, it is possibly that there are some cracks generated in the Y_2O_3/NiO particles, especially for those with large size. Agglomeration and particle growth commonly occur for bare MgH_2 after initial dehydrogenation, thus degrading the dehydrogenation performance. The low amount of addition of the Y_2O_3/NiO hybrid is insufficient in preventing the agglomeration

and particle growth. As a result, the second dehydrogenation temperature is higher than the initial one. Adding a high enough amount of the Y_2O_3/NiO hybrid can effectively prevent the agglomeration and particle growth of MgH_2, with the extra increased surface area, active sites, and therefore, the second dehydrogenation temperature is reduced.

Figure 9 shows the SEM images of the MgH_2-10 wt% Y_2O_3/NiO system at the dehydrogenation states of the initial cycle (a) and after 50 cycles (b). No obvious change in particle size is observed after the initial dehydrogenation (Figure 9a) compared with its as-milled sate (Figure 3h), whereas it is common that the particles of bare MgH_2 are severely agglomerated after dehydrogenation and hydrogenation cycles, as reported in literature [57,58]. This is also one of the main reasons for the capacity decay of MgH_2 during cycling. Figure 9c shows the TEM images of the dehydrogenation product of the MgH_2-10wt% Y_2O_3/NiO system after 50 cycles. It is seen that the dark-grey particles, which correspond to the Y_2O_3/NiO hybrid, are still uniformly distributed on the bright-grey matrix (Mg). It is obtained that either the spatial structure or the crystal structure of the Y_2O_3/NiO particles is mostly preserved during cycling. The Y_2O_3/NiO particles act as a barrier to inhibit the growth and agglomeration of MgH_2/Mg particles during cycling, favoring the cyclic stability.
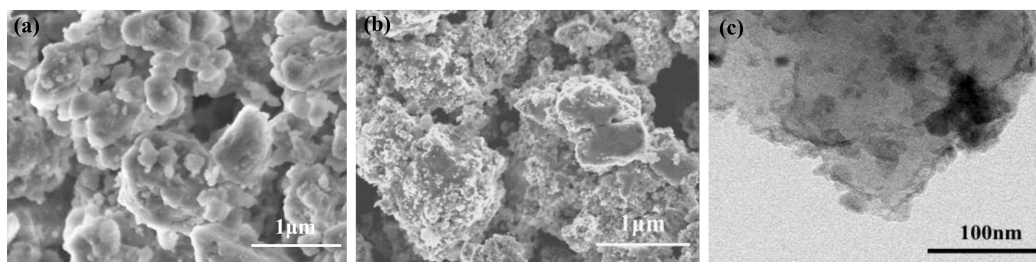

Figure 9. SEM images of the MgH_2-10 wt%Y_2O_3/NiO system after (**a**) 1st dehydrogenation and (**b**) 50th dehydrogenation. (**c**) A TEM image of the system at the state of 50th dehydrogenation.

To further understand the role of the intersected Y_2O_3/NiO hybrid on the hydrogen storage of MgH_2, the dehydrogenation and hydrogenation properties of the MgH_2-10 wt% Y_2O_3/NiO system are further compared with two reference systems, which are added with 10 wt% of commercial Y_2O_3 and NiO, respectively, prepared by the same ball-milling regime, which are performed for non-isothermal dehydrogenation and hydrogenation. The result (Figure S6) shows that the MgH_2-10 wt% Y_2O_3/NiO system has superior dehydrogenation and hydrogenation properties to the two reference systems, demonstrating that there is a synergistic catalytic effect between Y_2O_3 and NiO on the hydrogen storage of MgH_2.

To sum up, the introduction of the intersected Y_2O_3/NiO hybrid into MgH_2 significantly reduces the de-/hydrogenation temperatures and enhances the hydrogen sorption rate. As the intrinsic high hardness of the metal oxides of Y_2O_3 and NiO, and also the hollow structure of the hybrid with thin thickness of the shell, the hybrid serves as auxiliary abrasive agents reducing the particle size of MgH_2 during ball milling after it is crushed at the initial milling process. Thus, the particle size of MgH_2 is significantly reduced by the introduction of Y_2O_3/NiO, which is much smaller than that of the bare MgH_2 performed by the same milling process. The crushed Y_2O_3/NiO fragments are further ground to nanosized particles and uniformly dispersed in the MgH_2 matrix, acting as highly effective bidirectional catalyst to both dehydrogenation and hydrogenation of MgH_2.

From the present experiments, the amount of 10 wt% is suggested to be an optimized value for the addition of the intersected Y_2O_3/NiO hybrid, as obtained from Figure 4, for the dehydrogenation and hydrogenation of MgH_2-x wt% Y_2O_3/NiO systems. The catalytic effect is insufficient for the less amount of Y_2O_3/NiO introduction, and too much amount of Y_2O_3/NiO introduction results in obvious decrease in hydrogen storage capacity. The crystal structure and morphology of the Y_2O_3/NiO hybrid are almost maintained

during ball milling process and after long-term cycling (for 50 cycles, as shown in Figure 6). The stable structure of the Y_2O_3/NiO hybrid provides a long-term catalytic effect on the hydrogen storage of MgH_2. In terms of kinetic properties, as reported [40], the dissociation of the molecular hydrogen adsorbed on the surface of the metal oxide catalysts can be facilitated by the high-density defects introduced on the surface of hard oxides by ball milling, thus proving superior catalysis.

5. Conclusions

A novel intersected Y_2O_3/NiO hybrid with the morphology of hollow nanospheres is prepared, which shows bidirectional catalysis for MgH_2 hydrogen storage. The dehydrogenation temperature is significantly reduced by the introduction of the hybrid, where an increasing reduction is obtained with the increasing addition of the hybrid from 2 to 10 wt%, but the reduction becomes limited when the addition is further increased to 12 wt%. With an addition of 10 wt% Y_2O_3/NiO hybrid, MgH_2 shows an overall optimized hydrogen storage performance. It initiates the dehydrogenation at 220 °C and reaches the peak at 277 °C for the first dehydrogenation, and notably, the second desorption peak temperature is further reduced to 261 °C, which is lower by 125 °C compared with that of the bare MgH_2, and 6.6 wt% H_2 is desorbed at 275 °C within 60 min. The hydrogenation takes place at almost room temperature, and 4.2 wt% H_2 can be absorbed at 150 °C within 50 min. The apparent activation energy of dehydrogenation of MgH_2 is significantly lowered by the addition of the hybrid, which contributes to the improved reaction kinetics. A dehydrogenation capacity of 5.2 wt% is maintained after 50 cycles at a moderate cyclic condition, corresponding to the capacity retention of 79.2%. The crystal structure and distribution of the Y_2O_3/NiO hybrid are almost maintained during cycling, and the hybrid inhibits the agglomeration of MgH_2 particles, which all contribute to the favorable cyclic stability of MgH_2.

Author Contributions: Most of the experimental work, original draft preparation, and modification, Y.L. (Yushan Liu); methodology for experiments, manuscript review and editing, Z.L. and S.W.; conceptualization and data analysis, resources, project administration, funding acquisition, H.P. and M.G.; data analysis, W.S.; formal analysis, Y.L. (Yongfeng Liu) All authors have read and agreed to the published version of the manuscript. Authors also thank Na Zheng at State Key Laboratory of Chemical Engineering in Zhejiang University for performing SEM and EDS.

Institutional Review Board Statement: Not applicable.

Informed Consent Statement: Not applicable.

Data Availability Statement: Not applicable.

Conflicts of Interest: The authors declare no conflict of interest.

References

1. Schlapbach, L.; Züttel, A. Hydrogen-storage materials for mobile applications. *Nature* **2001**, *414*, 353–358. [CrossRef] [PubMed]
2. Yu, X.B.; Tang, Z.W.; Sun, D.L.; Ouyang, L.Z.; Zhu, M. Recent advances and remaining challenges of nanostructured materials for hydrogen storage applications. *Prog. Mater. Sci.* **2017**, *88*, 1–48. [CrossRef]
3. Wang, K.; Zhang, X.; Ren, Z.H.; Zhang, X.L.; Hu, J.J.; Gao, M.X.; Pan, H.G.; Liu, Y.F. Nitrogen-stimulated superior catalytic activity of niobium oxide for fast full hydrogenation of magnesium at ambient temperature. *Energy Storage. Mater.* **2019**, *23*, 79–87. [CrossRef]
4. Zhao, L.; Xu, F.; Zhang, C.C.; Wang, Z.Y.; Ju, H.Y.; Gao, X.; Zhang, X.X.; Sun, L.X.; Liu, Z.W. Enhanced hydrogen storage of alanates: Recent progress and future perspectives. *Prog. Nat. Sci. Mater. Int.* **2021**, *31*, 151–165. [CrossRef]
5. Hardian, R.; Pistidda, C.; Chaudhary, A.L.; Capurso, G.; Gizer, G.; Cao, H.; Milanese, C.; Girella, A.; Santoru, A.; Yigit, D.; et al. Waste Mg-Al based alloys for hydrogen storage. *Int. J. Hydrogen Energy* **2018**, *43*, 16738–16748. [CrossRef]
6. El-Eskandarany, M.S.; Ali, N.; Al-Salem, S.M. Solid-state conversion of magnesium waste to advanced hydrogen-storage nanopowder particles. *Nanomaterials* **2020**, *10*, 11–21. [CrossRef]
7. Selvam, P.; Viswanathan, B.; Swamy, C.S.; Srinivasan, V. Magnesium and magnesium alloy hydrides. *Int. J. Hydrogen Energy* **1986**, *11*, 169–192. [CrossRef]
8. Liu, H.Z.; Lu, C.L.; Wang, X.C.; Xu, L.; Huang, X.T.; Wang, X.H.; Ning, H.; Lan, Z.Q.; Guo, J. Combinations of V_2C and Ti_3C_2 MXenes for Boosting the Hydrogen Storage Performances of MgH_2. *ACS Appl. Mater. Interfaces* **2021**, *13*, 13235–13247. [CrossRef]
9. Kan, H.M.; Zhang, N.; Wang, X.Y. Al-Mg Alloy powders for hydrogen storage. *Adv. Mat. Res.* **2012**, *550–553*, 497–501. [CrossRef]
10. Wen, J.; de Rango, P.; Allain, N.; Laversenne, L.; Grosdidier, T. Improving hydrogen storage performance of Mg-based alloy through microstructure optimization. *J. Power Sources* **2020**, *480*, 228823. [CrossRef]
11. Hou, J.; Liu, Z.B.; Zhu, Y.F.; Fei, J.F.; Song, Y.T.; Zhang, Y.; Zhang, J.G.; Liu, Y.N.; Chen, Q.X.; Li, L.Q. Electrochemical hydrogen storage performance of Mg_3GeNi_2 alloy. *Intermetallics* **2020**, *127*, 106961. [CrossRef]
12. Zhang, Y.H.; Wei, W.; Zhang, W.; Yuan, Z.M.; Gao, J.L.; Qi, Y.; Ren, H.P. Effect of milling duration on hydrogen storage thermodynamics and kinetics of Mg-based alloy. *Int. J. Hydrogen Energy* **2020**, *45*, 33832–33845. [CrossRef]
13. Hou, Z.H.; Zhang, W.; Wei, X.; Yuan, Z.M.; Ge, Q.L. Hydrogen storage behavior of nanocrystalline and amorphous Mg-Ni-Cu-La alloys. *RSC Adv.* **2020**, *10*, 33103–33111. [CrossRef]
14. Yong, H.; Guo, S.H.; Yuan, Z.M.; Qi, Y.; Zhao, D.L.; Zhang, Y.H. Catalytic effect of in situ formed Mg_2Ni and REH_x (RE: Ce and Y) on thermodynamics and kinetics of Mg-RE-Ni hydrogen storage alloy. *Renew. Energy* **2020**, *157*, 828–839. [CrossRef]
15. Zhang, Y.H.; Zhang, W.; Gao, J.L.; Wei, X.; Zhai, T.T.; Cai, Y. Improved hydrogen storage kinetics of Mg-based alloys by substituting La with Sm. *Int. J. Hydrogen Energy* **2020**, *45*, 21588–21599. [CrossRef]
16. De Rango, P.; Wen, J.; Skryabina, N.; Laversenne, L.; Fruchart, D.; Borges, M. Hydrogen Storage Properties of Mg-Ni Alloys Processed by Fast Forging. *Energies* **2020**, *13*, 3509. [CrossRef]
17. Xie, L.S.; Xu, M. Improved Absorption and Desorption Kinetics of Mg-Ni-Ce Alloy Activated under Elevated Hydrogen Pressure. *Mater. Trans.* **2020**, *61*, 534–539. [CrossRef]
18. Zhang, X.L.; Liu, Y.F.; Zhang, X.; Hu, J.J.; Gao, M.X.; Pan, H.G. Empowering hydrogen storage performance of MgH_2 by nanoengineering and nanocatalysis. *Mater. Today Nano* **2020**, *9*, 100064. [CrossRef]
19. Ma, Z.W.; Panda, S.; Zhang, Q.Y.; Sun, F.Z.; Khan, D.; Ding, W.J.; Zou, J.X. Improving hydrogen sorption performances of MgH_2 through nanoconfinement in a mesoporous CoS nano-boxes scaffold. *Chem. Eng. J.* **2021**, *406*, 126790. [CrossRef]
20. Liang, H.; Chen, D.; Chen, M.; Li, W.; Snyders, R. Study of the synthesis of PMMA-Mg nanocomposite for hydrogen storage application. *Int. J. Hydrogen Energy* **2020**, *45*, 4743–4753. [CrossRef]
21. Zhang, X.; Liu, Y.; Ren, Z.; Zhang, X.; Hu, J.; Huang, Z.; Lu, Y.; Gao, M.; Pan, H. Realizing 6.7 wt% reversible storage of hydrogen at ambient temperature with non-confined ultrafine magnesium hydrides. *Energy Environ. Sci.* **2021**, *14*, 2302–2313. [CrossRef]
22. Shi, R.; Zhang, J.G.; Zhu, Y.F.; Liu, Y.N.; Hu, X.H.; Zhang, Y.; Su, W.; Li, L.Q. Synergistic Catalytic Mechanism between Ni and Carbon Aerogel for Dehydrogenation of Mg-Based Hydrides. *Energy Fuels* **2020**, *34*, 10232–10240. [CrossRef]
23. Pandey, A.P.; Bhatnagar, A.; Shukla, V.; Soni, P.K.; Singh, S.; Verma, S.K.; Shaneeth, M.; Sekkar, V.; Srivastava, O.N. Hydrogen storage properties of carbon aerogel synthesized by ambient pressure drying using new catalyst triethylamine. *Int. J. Hydrog. Energy* **2020**, *45*, 30818–30827. [CrossRef]
24. Ghaani, M.R.; Alam, M.; Catti, M.; English, N.J. In Situ Formation of Metal Hydrides Inside Carbon Aerogel Frameworks for Hydrogen Storage Applications. *Carbon Res.* **2020**, *6*, 38. [CrossRef]
25. Zhou, C.Q.; Peng, Y.Y.; Zhang, Q.G. Growth kinetics of MgH_2 nanocrystallites prepared by ball milling. *J. Mater. Sci. Technol.* **2020**, *50*, 178–183. [CrossRef]
26. Gattia, D.M.; Jangir, M.; Jain, I.P. Study on nanostructured MgH_2 with Fe and its oxides for hydrogen storage applications. *J. Alloys Compd.* **2019**, *801*, 188–191. [CrossRef]

27. Ding, Z.M.; Fu, Y.K.; Zhang, L.; Rodriguez-Perez, I.A.; Zhang, H.M.; Wang, W.F.; Li, Y.; Han, S.M. Improve hydrogen sorption kinetics of MgH_2 by doping carbon-encapsulated iron-nickel nanoparticles. *J. Alloys Compd.* **2020**, *843*, 156035. [CrossRef]

28. Zhu, W.; Panda, S.; Lu, C.; Ma, Z.W.; Khan, D.; Dong, J.J.; Sun, F.Z.; Xu, H.; Zhang, Q.Y.; Zou, J.X. Using a Self-Assembled Two-Dimensional MXene-Based Catalyst (2D-Ni@Ti_3C_2) to Enhance Hydrogen Storage Properties of MgH_2. *ACS Appl. Mater. Interfaces* **2020**, *12*, 50333–50343. [CrossRef]

29. Biasetti Andrés, T.; Zélis Luis, M.; Marcos, M. Differences in the heterogeneous nature of hydriding/dehydriding kinetics of MgH_2 - TiH_2 nanocomposites. *Int. J. Hydrogen Energy* **2020**, *45*, 27421–27433. [CrossRef]

30. Zhang, L.C.; Wang, K.; Liu, Y.F.; Zhang, X.; Hu, J.J.; Gao, M.X.; Pan, H.G. Highly active multivalent multielement catalysts derived from hierarchical porous $TiNb_2O_7$ nanospheres for the reversible hydrogen storage of MgH_2. *Nano Res.* **2021**, *14*, 148–156. [CrossRef]

31. Fu, Y.; Ding, Z.; Zhang, L.; Zhang, H.; Wang, W.; Li, Y.; Han, S. Catalytic effect of a novel $MgC_{0.5}Co_3$ compound on the dehydrogenation of MgH_2. *Prog. Nat. Sci. Mater. Int.* **2021**, *31*, 264–269. [CrossRef]

32. Ismail, M.; Yahya, M.S.; Sazelee, N.A.; Ali, N.A.; Yap, F.A.H.; Mustafa, N.S. The effect of K_2SiF_6 on the MgH_2 hydrogen storage properties. *J. Magnes. Alloys* **2020**, *8*, 832–840. [CrossRef]

33. Gao, S.C.; Wang, H.; Wang, X.H.; Liu, H.Z.; He, T.; Wang, Y.Y.; Wu, C.; Li, S.Q.; Yan, M. $MoSe_2$ hollow nanospheres decorated with $FeNi_3$ nanoparticles for enhancing the hydrogen storage properties of MgH_2. *J. Alloys Compd.* **2020**, *830*, 154631. [CrossRef]

34. Ouyang, L.Z.; Cao, Z.J.; Wang, H.; Liu, J.W.; Sun, D.L.; Zhang, Q.A.; Zhu, M. Dual-tuning effect of In on the thermodynamic and kinetic properties of Mg_2Ni dehydrogenation. *Int. J. Hydrogen Energy* **2013**, *38*, 8881–8887. [CrossRef]

35. Sazelee, N.A.; Idris, N.H.; Din, M.F.M.; Yahya, M.S.; Ali, N.A.; Ismail, M. $LaFeO_3$ synthesized by solid-state method for enhanced sorption properties of MgH_2. *Results Phys.* **2020**, *16*, 102844. [CrossRef]

36. Wagemans, R.W.P.; Van Lenthe, J.H.; De Jongh, P.E.; Van Dillen, A.J.; De Jong, K.P. Hydrogen storage in magnesium clusters: Quantum chemical study. *J. Am. Chem. Soc.* **2005**, *127*, 16675–16680. [CrossRef]

37. Zhu, X.L.; Pei, L.C.; Zhao, Z.Y.; Liu, B.Z.; Han, S.M.; Wang, R.B. The catalysis mechanism of La hydrides on hydrogen storage properties of MgH_2 in MgH_2 + x wt.% LaH_3 (x=0, 10, 20, and 30) composites. *J. Alloys Compd.* **2013**, *557*, 64–69. [CrossRef]

38. Liang, G.; Huot, J.; Boily, S.; Van Neste, A.; Schulz, R. Catalytic effect of transition metals on hydrogen sorption in nanocrystalline ball milled MgH_2–Tm (Tm = Ti, V, Mn, Fe and Ni) systems. *J. Alloys Compd.* **1999**, *292*, 247–252. [CrossRef]

39. Barkhordarian, G.; Klassen, T.; Bormann, R. Effect of Nb_2O_5 content on hydrogen reaction kinetics of Mg. *J. Alloys Compd.* **2004**, *364*, 242–246. [CrossRef]

40. Oelerich, W.; Klassen, T.; Bormann, R. Metal oxides as catalysts for improved hydrogen sorption in nanocrystalline Mg-based materials. *J. Alloys Compd.* **2001**, *315*, 237–242. [CrossRef]

41. Cui, J.; Liu, J.W.; Wang, H.; Ouyang, L.Z.; Sun, D.L.; Zhu, M.; Yao, X.D. Mg–TM (TM: Ti, Nb, V, Co, Mo or Ni) core–shell like nanostructures: Synthesis, hydrogen storage performance and catalytic mechanism. *J. Mater. Chem. A* **2014**, *2*, 9645. [CrossRef]

42. Chen, J.; Xia, G.L.; Guo, Z.P.; Huang, Z.G.; Liu, H.K.; Yu, X.B. Porous Ni nanofibers with enhanced catalytic effect on the hydrogen storage performance of MgH_2. *J. Mater. Chem. A* **2015**, *3*, 15843. [CrossRef]

43. Long, S.; Zou, J.X.; Chen, X.; Zeng, X.Q.; Ding, W.J. A comparison study of Mg–Y_2O_3 and Mg–Y hydrogen storage composite powders prepared through arc plasma method. *J. Alloys Compd.* **2014**, *615*, S684–S688. [CrossRef]

44. Lei, Z.L.; Liu, Z.Y.; Chen, Y.B. Cyclic hydrogen storage properties of Mg milled with nickel nano-powders and NiO. *J. Alloys Compd.* **2009**, *470*, 470–472.

45. Rajabpour, F.; Raygan, S.; Abdizadeh, H. The synergistic effect of catalysts on hydrogen desorption properties of MgH_2–TiO_2–NiO nanocomposite. *Mater. Renew. Sustain. Energy* **2016**, *5*, 20. [CrossRef]

46. Sadhasivam, T.; Hudson, M.S.L.; Pandey, S.K.; Bhatnagar, A.; Singh, M.K.; Gurunathan, K.; Srivastava, O.N. Effects of nano size mischmetal and its oxide on improving the hydrogen sorption behaviour of MgH_2. *Int. J. Hydrogen Energy* **2013**, *38*, 7353–7362. [CrossRef]

47. Zhong, H.C.; Huang, Y.S.; Du, Z.Y.; Lin, H.J.; Lu, X.J.; Cao, C.Y.; Chen, J.H.; Dai, L.Y. Enhanced Hydrogen Ab/De-sorption of Mg(Zn) solid solution alloy catalyzed by YH_2/Y_2O_3 nanocomposite. *Int. J. Hydrogen Energy* **2020**, *45*, 27404–27412. [CrossRef]

48. Kissinger, H.E. Reaction Kinetics in Differential Thermal Analysis. *Anal. Chem.* **1957**, *29*, 1702–1706. [CrossRef]

49. Lu, C.; Ma, Y.; Li, F.; Zhu, H.; Zeng, X.; Ding, W.; Deng, T.; Wu, J.; Zou, J. Visualization of fast "hydrogen pump" in core-shell nanostructured Mg@Pt through hydrogen-stabilized Mg_3Pt. *J. Mater. Chem. A* **2019**, *7*, 14629–14637. [CrossRef]

50. Sun, Z.; Zhang, L.; Yan, N.; Zheng, J.; Bian, T.; Yang, Z.; Su, S. Realizing hydrogen de/absorption under low temperature for MgH_2 by doping Mn-based catalysts. *Nanomaterials* **2020**, *10*, 1–11. [CrossRef]

51. Singh, S.; Bhatnagar, A.; Shukla, V.; Vishwakarma, A.K.; Soni, P.K.; Verma, S.K.; Shaz, M.A.; Sinha, A.S.K.; Srivastava, O.N. Ternary transition metal alloy FeCoNi nanoparticles on graphene as new catalyst for hydrogen sorption in MgH_2. *Int. J. Hydrogen Energy* **2020**, *45*, 774–786. [CrossRef]

52. Ismail, M. Effect of adding different percentages of $HfCl_4$ on the hydrogen storage properties of MgH_2. *Int. J. Hydrogen Energy* **2021**, *46*, 8621–8628. [CrossRef]

53. Hu, M.; Xie, X.; Chen, M.; Zhu, C.; Liu, T. TiC_X-decorated Mg nanoparticles confined in carbon shell: Preparation and catalytic mechanism for hydrogen storage. *J. Alloys Compd.* **2020**, *817*, 152813. [CrossRef]

54. Gao, S.; Wang, X.; Liu, H.; He, T.; Wang, Y.; Li, S.; Yan, M. Effects of nano-composites (FeB, FeB/CNTs) on hydrogen storage properties of MgH_2. *J. Power Sources* **2019**, *438*, 227006. [CrossRef]

55. Zhang, Q.; Zang, L.; Huang, Y.; Gao, P.; Jiao, L.; Yuan, H.; Wang, Y. Improved hydrogen storage properties of MgH$_2$ with Ni-based compounds. *Int. J. Hydrogen Energy* **2017**, *42*, 24247–24255. [CrossRef]

56. Han, Z.Y.; Yeboah, M.L.; Jiang, R.Q.; Li, X.Y.; Zhou, S.X. Hybrid activation mechanism of thermal annealing for hydrogen storage of magnesium based on experimental evidence and theoretical validation. *Appl. Surf. Sci.* **2020**, *504*, 144491. [CrossRef]

57. Liu, M.; Xiao, X.; Zhao, S.; Saremi-Yarahmadi, S.; Chen, M.; Zheng, J.; Li, S.; Chen, L. ZIF-67 derived Co@CNTs nanoparticles: Remarkably improved hydrogen storage properties of MgH$_2$ and synergetic catalysis mechanism. *Int. J. Hydrogen Energy* **2019**, *44*, 1059–1069. [CrossRef]

58. Xia, G.; Tan, Y.; Chen, X.; Sun, D.; Guo, Z.; Liu, H.; Ouyang, L.; Zhu, M.; Yu, X. Monodisperse Magnesium Hydride Nanoparticles Uniformly Self-Assembled on Graphene. *Adv. Mater.* **2015**, *27*, 5981–5988. [CrossRef] [PubMed]